



Delft University of Technology

Robust Traveling Wave-based Protection Scheme For Multiterminal DC Grids

Liu, Le; Lekic, Aleksandra; Popov, Marjan

DOI

[10.1109/TPWRD.2023.3265748](https://doi.org/10.1109/TPWRD.2023.3265748)

Publication date

2023

Document Version

Final published version

Published in

IEEE Transactions on Power Delivery

Citation (APA)

Liu, L., Lekic, A., & Popov, M. (2023). Robust Traveling Wave-based Protection Scheme For Multiterminal DC Grids. *IEEE Transactions on Power Delivery*, 38(5), 3117-3129.
<https://doi.org/10.1109/TPWRD.2023.3265748>

Important note

To cite this publication, please use the final published version (if applicable).
Please check the document version above.

Copyright

Other than for strictly personal use, it is not permitted to download, forward or distribute the text or part of it, without the consent of the author(s) and/or copyright holder(s), unless the work is under an open content license such as Creative Commons.

Takedown policy

Please contact us and provide details if you believe this document breaches copyrights.
We will remove access to the work immediately and investigate your claim.

Green Open Access added to TU Delft Institutional Repository

'You share, we take care!' - Taverne project

<https://www.openaccess.nl/en/you-share-we-take-care>

Otherwise as indicated in the copyright section: the publisher is the copyright holder of this work and the author uses the Dutch legislation to make this work public.

Robust Traveling Wave-Based Protection Scheme for Multiterminal DC Grids

Le Liu , *Student Member, IEEE*, Aleksandra Lekić , *Senior Member, IEEE*, and Marjan Popov , *Fellow, IEEE*

Abstract—The DC transmission line protection technology is crucial for the development of multi-terminal Voltage Source Converter (VSC)-based HVDC systems. This article proposes a robust non-unit traveling wave protection (TWP), which deals with the DC fault area identification and fault type discrimination for high impedance fault conditions. The authors applied the traveling wave (TW) reflection and refraction method for the line-mode network. The distinctive features of high-frequency components contained in the line-mode and pole-mode voltage TWs at different relay units are used for the algorithm modeling. Discrete Wavelet Transform (DWT) is selected as the time-frequency analysis tool. The performed simulations are conducted for a four-terminal VSC-HVDC system, and validate the protection feasibility and robustness. More precisely, the proposed protection scheme identifies the internal and external DC faults within 2 ms, and provides correct operation during high-impedance faults (HIF) with a 25 dB level noise interference. This protection scheme makes use of a VSC-assisted resonant current (VARC) direct current circuit breaker (DCCB), that successfully interrupts the fault currents in less than 10 ms after the fault inception. The authors also comprehensively compared the proposed scheme with the existing methods. The obtained results show that the proposed protection scheme is superior in terms of sensitivity and selectivity performance.

Index Terms—Non-unit protection, modular multi-level converter (MMC), high voltage direct current (HVDC), DC circuit breakers (DCCB), discrete wavelet transform (DWT).

I. INTRODUCTION

VSC based high voltage direct current (HVDC) power systems are recognized as one of the best solutions to access fluctuating renewable power sources to transport electricity over long distances [1]. They are widely applied in modern industry to connect onshore and offshore wind farms. Examples of this type of HVDC systems are the BorWin, DolWin, and NorNed offshore projects in Northsea and the Zhangbei, Wudongde, and Zhoushan multi-terminal HVDC (MTDC) grids in China.

In case of a DC fault on HVDC transmission lines, the DC voltage suffers a deep sag, the fault current increases promptly to the peak value after several milliseconds, which may easily

damage the power electronic device, and may lead to a collapse of the entire system. Thus, it is crucial to implement a fast, selective, and reliable DC fault protection technology. Currently, substantive research has been conducted in the field of DC line protection. Present methodologies can be classified into two categories: unit- and non-unit protections.

A. Unit Protection Methods

Unit protection relies on communication channels to exchange measurement data between the relays located at both ends of a transmission line. Several methods for unit protection have been proposed, including those based on current differential [2], impedance differential [3], waveform similarity [4], and others. The key advantage of this protection category is its absolute selectivity. However, unit protection requires precise and synchronized measurement data from multiple relay terminals, which can be challenging to achieve over long distances (e.g., 1489 km in the Wudongde project) or in the event of communication network failures. Data exchange between relays causes delays in detecting faults and tripping DCCBs. Additionally, implementing and maintaining unit protection inquires substantial costs due to the need for specialized equipment and communication channels.

B. Non-Unit Protection Methods

By contrast, another category of non-unit protection does not require a communication channel and can identify the faulty line with only local measurements.

1) *Time Domain TW-Based Protections*: In [5], a fault detection scheme is proposed by applying the locally measured rate of change of voltage (ROCOV). To enhance the performance of fault type discrimination, the protection in [6] was achieved by computing the ratio of transient voltage (ROTV). The undervoltage, DC voltage derivative, and directional overcurrent criteria are used in combination to design the protection scheme [7]. Practical HVDC projects typically utilize the derivative of pole/ground-mode waves (P_{wave} , G_{wave}), or voltage/current-based TWPs [8], as the primary protections. Although these methods offer fast detection speeds and eliminate protection dead zones, they heavily rely on TW amplitudes, which impose low sensitivity under HIF and, as such are susceptible to noise.

2) *DC Inductor Voltage-Based Protections*: In practical MTDC systems, DC limiting inductors are often installed at each line terminal, forming a boundary around the DC transmission line. The protection schemes in [9], [10] detect faults using the

Manuscript received 10 November 2022; revised 22 February 2023; accepted 4 April 2023. Date of publication 12 April 2023; date of current version 25 September 2023. This work was supported in part by the Chinese Scholarship Council (CSC) under Grant 202006280010. Paper no. TPWRD-01677-2022. (Corresponding author: Marjan Popov.)

The authors are with the Faculty of Electrical Engineering, Mathematics and Computer Science, Delft University of Technology, CD 2628 Delft, The Netherlands (e-mail: l.liu-7@tudelft.nl; A.Lekic@tudelft.nl; M.Popov@tudelft.nl).

Color versions of one or more figures in this article are available at <https://doi.org/10.1109/TPWRD.2023.3265748>.

Digital Object Identifier 10.1109/TPWRD.2023.3265748

inductor voltage change rate and the inductor voltage differences between the negative and positive poles, respectively. However, the scheme in [9] cannot identify PTG faults, and the method in [10] fails to detect HIF [11]. Based on the modal-domain analysis, the method in [12] adopts the line-mode inductor voltage for the fault detection and zero-mode voltage for the fault type discrimination. Compared to time-domain TW-based methods, these methods are easy to implement, robust to noise interference, and do not require a high sampling frequency. However, the sensitivity performance under HIF could be further improved.

3) *Time Frequency Analyses-Based Protections*: The DC inductors attenuate specific harmonics and excessive high-frequency components at the line terminals. The significant presence of high-frequency components between the faulty and healthy lines can be utilized to identify faults. Various time-frequency analyses have been conducted for fault detection. Short-time Fourier Transform (SFFT) [13] and Fast Fourier Transform (FFT) [14] based protections have been proposed. Despite their fast processing speed, SFFT and FFT have a limited ability to capture time-frequency information, and SFFT's performance is restricted by a fixed window length and noise. The Stockwell transform (ST)-based protection [15] achieves high accuracy with a fast response and low computational burden. However, it requires further improvement in robustness against fault conditions. The authors of [16], [17] applied Hilbert Huang Transform (HHT) and empirical mode decomposition (EMD) to decompose the measured signals into data-sets with different frequency ranges for transient signal analysis. However, these methods are usually noise-sensitive. Besides, their resolution can be limited by the selection of intrinsic mode functions (IMFs), making them less suitable for industrial applications.

Compared to previous time-frequency analysis methods, the wavelet transform (WT) offers exceptional noise-filtering ability, enabling precise signal decomposition into distinct frequency components. It also delivers excellent time-frequency resolution with fast processing [11]. In [18], the current TWs are analyzed using the continuous wavelet transform (CWT), but it requires an extremely high sampling frequency (2 MHz) and additional synchronized devices. Moreover, the study does not include robustness tests for high-impedance faults. Similarly, previous works [19], [20] use WT to extract transient signal frequency components. However, they lack specific fault type discrimination in their protection schemes, and the sensitivity against HIF, maximum detectable 200 Ω , in [21] can be improved.

C. Main Contribution

Compared with the existing WT-based protection schemes, the novelty and the main contributions of our research are threefold. Firstly, the proposed protection scheme utilizes the characteristic of the transient high-frequency components contained in the fault-induced line-mode and the pole voltage TWs, identifying the DC fault area and discriminating the specific fault type in the MTDC system. Secondly, the proposed protection scheme improves the sensitivity performance in detecting HIF and provides the tripping signals to DCCB promptly. Thirdly,

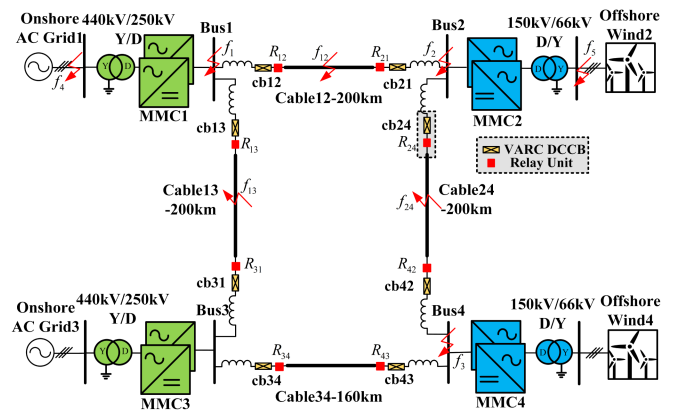


Fig. 1. Configuration of studied system.

the thresholds can be easily determined, and in this way, they can be easily implemented for other test models and real systems.

The rest of the paper is organized as follows. Section II outlines the offshore testing grid setup conditions in PSCAD/EMTDC. Section III presents the theoretical analysis of line-mode voltage traveling waves after a DC fault. Section IV describes the proposed protection scheme using DWT. Section V validates the performance of the protection scheme in the PSCAD environment. Finally, conclusions are elaborated in Section VI, which also refers to future work.

II. TEST SYSTEM SET UP

To demonstrate the performance of the proposed protection scheme, a ± 525 kV four-terminal meshed MMC-HVDC system with a bipolar configuration is modeled in PSCAD/EMTDC. MMC1 and MMC3 are grid-following control regulating the DC voltage and active power, and MMC2 and MMC4 are grid-forming control supporting the wind farm energy. The configuration of the MTDC system is shown in Fig. 1. At each end of the DC cable, two relay units (denoted in red) are installed on the positive and the negative poles, respectively. All relay units make use of the protection scheme explained in section IV. To obtain accurate transient responses, the transmission lines of the test system are simulated by applying a frequency-dependent cable model. The configuration of the cable model is based on CIGRE B4.57.

The VARC DCCBs are implemented at each cable terminal, following the approach proposed in [22]. The protection will trip the corresponding DCCBs to interrupt the fault currents if a fault is detected. The VARC DCCB makes use of a vacuum interrupter which has short arcing times normally in the range of microseconds. Thus, simulations are performed in PSCAD/EMTDC with a solution time step of 1 μ s [22] to ensure all important signals of VARC DCCB can be precisely monitored. The critical parameters in the current injection branch of the VARC DCCBs described in [22] are scaled for a 525 kV system and are presented in Table I, where L_p and C_p stand for the oscillating inductor and capacitor, respectively. $V_{in}C_p$ is the initial voltage across capacitor C_p . Particularly, the DC inductor, L_{dc} , is set to 120 mH to limit the rate of rise and peak value of

TABLE I
PARAMETERS OF VARC DCCB FOR 525 kV SYSTEM

Item	L_{dc} (mH)	L_p (μ H)	C_p (μ F)	Surge arrester (SA) rated voltage (kV)	$V_{in}C_p$ (kV)
320kV [22]	80	300	0.66	320/480	24
525kV	120	492.18	0.40	525/787.5	39.37

TABLE II
PARAMETERS OF THE FOUR-TERMINAL HVDC SYSTEM IN PSCAD

Item	MMC1&3	MMC2&4
Nominal system frequency (Hz)	50	50
MMC (one pole) rated capacity (MVA)	2000	2000
Transformer ratio (D/Y _n)	400/250	66/150
Transformer leakage inductance (p.u.)	0.18	0.18
Number of arm sub-module (SM)	175	175
Arm inductance L_{arm} (mH)	4.2	4.2
Capacitance of each SM C_{sm} (μ F)	15000	15000
On-state arm resistance R_{on} (Ω)	0.001361	0.001361
Arm resistance R_{arm} (Ω)	0.08	0.08
SM capacitor voltage rating (kV)	2.0	2.0
DC inductor L_{dc} (mH)	120	120

TABLE III
LINE- AND ZERO-MODE INITIAL VOLTAGES AT FAULT POINT [23]

Item	PTP	PTG	NTG
Δu_{F1}	$\frac{-\sqrt{2}U_f Z_{c(1)}}{Z_{c(1)}+R_f}$	$\frac{-\sqrt{2}U_f Z_{c(1)}}{Z_{c(1)}+Z_{c(0)}+4R_f}$	$\frac{-\sqrt{2}U_f Z_{c(1)}}{Z_{c(1)}+Z_{c(0)}+4R_f}$
Δu_{F0}	0	$\frac{-\sqrt{2}U_f Z_{c(0)}}{Z_{c(1)}+Z_{c(0)}+4R_f}$	$\frac{\sqrt{2}U_f Z_{c(0)}}{Z_{c(1)}+Z_{c(0)}+4R_f}$

the fault current, ensuring that the VARC DCCB can effectively interrupt the fault current.

A comprehensive list of the system parameters in a PSCAD/EMTDC environment can be found in Table II.

III. CHARACTERISTIC ANALYSIS OF HIGH-FREQUENCY COMPONENTS IN THE LINE-MODE AND POLE VOLTAGES

A. Initial Value of Line-Mode Voltage At Fault Point

In the symmetrical bipolar transmission line, the pole voltages u_p and u_n and currents i_p and i_n can be transformed into zero-mode u_0 , i_0 and line-mode components and u_1 , i_1 via:

$$\begin{bmatrix} u_0 \\ u_1 \end{bmatrix} = \frac{1}{\sqrt{2}} \begin{bmatrix} 1 & 1 \\ 1 & -1 \end{bmatrix} \begin{bmatrix} u_p \\ u_n \end{bmatrix}, \quad \begin{bmatrix} i_0 \\ i_1 \end{bmatrix} = \frac{1}{\sqrt{2}} \begin{bmatrix} 1 & 1 \\ 1 & -1 \end{bmatrix} \begin{bmatrix} i_p \\ i_n \end{bmatrix} \quad (1)$$

As such, the symmetrical bipolar transmission system can be represented as an independent line and a zero-mode network.

By combining the zero- and line-mode sequence network, the initial fault values of the line-mode and zero-mode voltages (Δu_{F1} , Δu_{F0}) at the fault point for a typical pole-to-pole fault (PTP), positive pole-to-ground (PTG) fault, and negative pole-to-ground (NTG) fault are listed in Table III, where U_f denotes the rated line voltage, R_f refers to fault resistance, $Z_{c(1)}$ and $Z_{c(0)}$ represent the line- and zero-mode characteristic impedances, respectively. For the used cable model, $Z_{c(1)} = 60.714 \Omega$, and $Z_{c(0)} = 169.587 \Omega$.

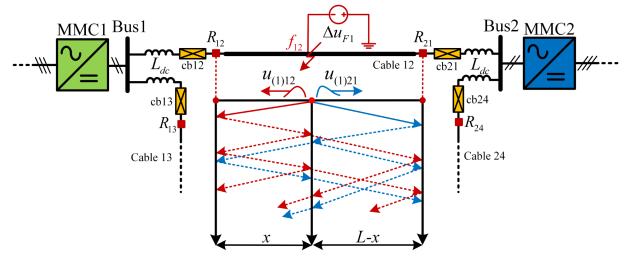


Fig. 2. Lattice diagram for a cable fault in the line-mode network.

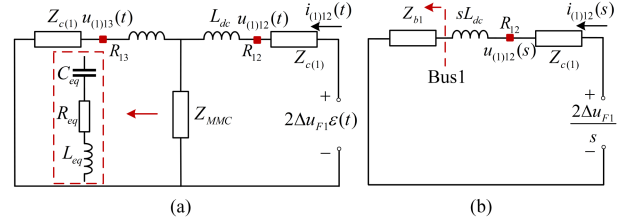


Fig. 3. (a) Peterson equivalent circuit; and (b) simplified circuit in S-domain.

In the subsequent analysis, the line-mode components are used to highlight the propagation characteristics of traveling waves for two reasons: 1) The zero-mode components cannot be used to distinguish PTP faults as they are always zero; 2) The line-mode components have smaller attenuation constants and higher propagation velocities compared to the zero-mode component.

B. Expression of Line-Mode Current At Internal and External Measuring Relays

1) *Simplified Fault Component Peterson Circuit in S-Domain:* For a case study, cable 12 in Fig. 1 is selected to be the faulty cable. Accordingly, R_{12} and R_{21} are the observed relays units. Fig. 2 describes the lattice diagram of an internal DC fault f_{12} in the line-mode network.

For a fault f_{12} in Fig. 2, the line-mode fault components of the Peterson equivalent circuit and its simplified circuit can be seen in Fig. 3. In Fig. 3(a), the voltage source is two times the initial voltage Δu_{F1} at the fault inception point. Z_{MMC} represents the equivalent impedance of an MMC converter, which is generally considered a series RLC circuit:

$$R_{eq} = \frac{2(R_{arm} + R_{on})}{3}, \quad L_{eq} = \frac{2L_{arm}}{3}, \quad C_{eq} = \frac{6C_{sm}}{N}, \quad (2)$$

where R_{eq} , L_{eq} , and C_{eq} represent the MMC equivalent resistance, inductance, and capacitance, respectively. As shown in Table II, $R_{eq} = 0.0542 \Omega$, $C_{eq} = 0.5142 \times 10^3 \mu\text{F}$, $L_{eq} = 2.8 \text{ mH}$ in the studied system.

By applying the Laplace transform to the circuit, the MMC impedance can be simplified to $Z_{MMC}(s) = 1/sC_{eq} + sL_{eq}$, as the impact of R_{eq} is negligible. The impact of VARC DCCB is neglected in Fig. 3(a) as the DCCB is not initialized by the protection before the measured line-mode voltage TW arrives at the relay. Therefore, the circuit in Fig. 3(a) can be simplified by

defining the equivalent impedance Z_{b1} at bus1 as:

$$Z_{b1} = \frac{(Z_{c(1)} + sL_{dc}) \left(\frac{1}{sC_{eq}} + sL_{eq} \right)}{Z_{c(1)} + sL_{dc} + \frac{1}{sC_{eq}} + sL_{eq}} \quad (3)$$

2) *Line-Mode Voltage TWs Measured at Internal Relay Units*: According to Fig. 3(b), one can obtain the S -domain expression for line-mode voltage $u_{(1)12}(s)$ as follows:

$$\begin{aligned} u_{(1)12}(s) &= \frac{2\Delta u_{F1}}{s} \left(1 - \frac{Z_{c(1)}}{Z_{c(1)} + sL_{dc} + Z_{b1}} \right) \\ &= \frac{2\Delta u_{F1}}{s} \left(1 - \frac{Z_{c(1)}(s - z_1)(s - z_2)}{(Z_{c(1)} + sL_{dc})(s - p_1)(s - p_2)} \right), \end{aligned} \quad (4)$$

where $z_1, z_2, p_1,$ and p_2 in (4) are calculated as follows:

$$\begin{cases} z_{1,2} = \frac{-Z_{c(1)}C_{eq} \pm \sqrt{(Z_{c(1)}C_{eq})^2 - 4C_{eq}(L_{dc} + L_{eq})}}{2C_{eq}(L_{dc} + L_{eq})}, \\ p_{1,2} = \frac{-Z_{c(1)}C_{eq} \pm \sqrt{(Z_{c(1)}C_{eq})^2 - 8C_{eq}(L_{dc} + 2L_{eq})}}{2C_{eq}(L_{dc} + 2L_{eq})}. \end{cases} \quad (5)$$

For the studied system, the following parameters are applied: $L_{dc} = 120$ mH, $Z_{c(1)} = 60.714 \Omega$. As such, one can obtain that: $Z_{c(1)}^2 C_{eq}^2 = 947.63 \times 10^6 \gg 8C_{eq}(2L_{eq} + L_{dc}) = 516.67 \times 10^3 > 4C_{eq}(L_{dc} + L_{eq}) = 252.57 \times 10^3$. Accordingly, the roots in (5) can be simplified as: $z_1 = p_1 \approx 0, z_2 \approx -Z_{c(1)}/(L_{dc} + L_{eq}), p_2 \approx -Z_{c(1)}/(L_{dc} + 2L_{eq})$. Thereby, we have:

$$u_{(1)12}(s) = \frac{2\Delta u_{F1}}{s} \left(1 - \frac{Z_{c(1)} \left(s + \frac{Z_{c(1)}}{L_{dc} + L_{eq}} \right)}{(Z_{c(1)} + sL_{dc}) \left(s + \frac{Z_{c(1)}}{L_{dc} + 2L_{eq}} \right)} \right). \quad (6)$$

Given that $L_{dc} + L_{eq} = 122.8$ mH $\approx L_{dc} + 2L_{eq} = 125.6$ mH. We can further simplify (6) as:

$$u_{(1)12}(s) = \frac{2\Delta u_{F1}}{s} \cdot \left(1 - \frac{Z_{c(1)}}{Z_{c(1)} + sL_{dc}} \right). \quad (7)$$

To describe the attenuation effect of TWs along the traveling distance x , an exponential propagation function $e^{-\Gamma(s)x}$ [24] is introduced:

$$e^{-\Gamma_1(s)x} = e^{-\sqrt{(r_0 + sl_0)(g_0 + sc_0)}x} \approx \frac{1 - k_1 x}{1 + s \cdot \tau_1 x} \cdot e^{-s \cdot \frac{x}{v_{(1)}}}, \quad (8)$$

where $\Gamma_1(s)x$ is the line-mode TW propagation coefficient representing the attenuation effect and phase shift along with traveling distance x . r_0, l_0 are the per-unit line resistance and inductance, and g_0, c_0 are the per-unit line-to-ground conductance and capacitance, respectively. $v_{(1)}$ is the propagation velocity of the line-mode TWs in the cable. The values for k_1 and τ_1 in [25] are modified into $k_1 = 5 \times 10^{-5}/\text{km}$, and $\tau_1 = 1.5 \times 10^{-8}\text{s}/\text{km}$ considering the different distributed parameters between the DC cable and overhead line.

As such, the expression of $u_{(1)12}(s)$ with the fault distance x becomes:

$$u_{(1)12}(s) = \frac{2\Delta u_{F1}}{s} \left(1 - \frac{Z_{c(1)}}{Z_{c(1)} + sL_{dc}} \right) \frac{1 - k_1 x}{1 + s\tau_1 x} e^{-s \cdot \frac{x}{v_{(1)}}}. \quad (9)$$

Due to the symmetrical system topology, the expression for $u_{(1)21}(s)$ monitored at relay unit R_{21} can be obtained by replacing x with $(L - x)$ in (9) as follows:

$$u_{(1)21}(s) = \frac{2\Delta u_{F1}}{s} \left(1 - \frac{Z_{c(1)}}{Z_{c(1)} + sL_{dc}} \right) \frac{1 - k_1(L - x)}{1 + s\tau_1(L - x)} e^{-s \cdot \frac{L-x}{v_{(1)}}}. \quad (10)$$

To obtain the time-domain expression for $u_{(1)12}(t)$, the $u_{(1)12}(s)$ in (9) could be rewritten as:

$$u_{(1)12}(s) = \left(\frac{A_1}{s + B_1} + \frac{A_2}{s + B_2} \right) \cdot e^{-s \cdot T_{d0}}, \quad (11)$$

where in (11), the items are calculated as follows:

$$\begin{cases} A_1 = \frac{2\Delta u_{F1}(1 - k_1 x)L_{dc}}{L_{dc} - Z_{c(1)}\tau_1 x}, B_1 = \frac{Z_{c(1)}}{L_{dc}}, B_2 = \frac{1}{\tau_1 x}, \\ A_2 = \frac{2\Delta u_{F1}(1 - k_1 x)L_{dc}}{Z_{c(1)}\tau_1 x - L_{dc}}, T_{d0} = x/v_{(1)}. \end{cases} \quad (12)$$

Using the *Inverse Laplace Transform*, we obtain the following time-domain expression for $u_{(1)12}(t)$:

$$\begin{aligned} u_{(1)12}(t) &= \left(A_1 e^{-B_1(t - T_{d0})} + A_2 e^{-B_2(t - T_{d0})} \right) \varepsilon(t - T_{d0}) \\ &= \frac{2\Delta u_{F1}(1 - k_1 x)L_{dc}}{L_{dc} - Z_{c(1)}\tau_1 x} \left(e^{-\frac{t - T_{d0}}{L_{dc}/Z_{c(1)}}} - e^{-\frac{t - T_{d0}}{\tau_1 x}} \right) \varepsilon(t - T_{d0}). \end{aligned} \quad (13)$$

It is evident that $u_{(1)12}(t)$ contains two exponential functions $A_1 e^{-B_1(t - T_{d0})}$ and $A_2 e^{-B_2(t - T_{d0})}$, resulting from the line boundary characteristics and line propagation characteristics, respectively. Combining (13) and Table III, the amplitude of $u_{(1)12}(t)$ is affected by fault type, fault distance x and fault resistance R_f , and size of L_{dc} . Due to the symmetrical configuration, the above-analyzed features apply to line-mode voltage TWs measured in cable24 and cable34.

3) *Line-Mode Voltage TWs Measured At External Relay Units*: A part of the TWs initiated by f_{12} at the fault point propagates into the neighbouring cables. According to Fig. 3(a), $i_{(1)12}(s)$ can be expressed as:

$$i_{(1)12}(s) = \frac{2\Delta u_{F1}}{s(Z_{c(1)} + sL_{dc})} \cdot \frac{1 - k_1 x}{1 + s\tau_1 x} \cdot e^{-s \cdot \frac{x}{v_{(1)}}}. \quad (14)$$

Accordingly, $u_{(1)13}(s)$ measured at R_{13} is calculated as:

$$\begin{aligned} u_{(1)13}(s) &= \left(\frac{2\Delta u_{F1}}{s} - (Z_{c(1)} + sL_{dc})i_{(1)12}(s) \right) \frac{Z_{c(1)}}{Z_{c(1)} + sL_{dc}} \\ &= \frac{2\Delta u_{F1}Z_{c(1)}}{s(Z_{c(1)} + sL_{dc})} \left(1 - \frac{1 - k_1 x}{1 + s\tau_1 x} e^{-s \cdot \frac{x}{v_{(1)}}} \right). \end{aligned} \quad (15)$$

C. Difference of High-Frequency Components in Internal and External Line-Mode Voltage TWs

By Combining (9) and (15), the transfer function $H(s)$ representing the boundary effects of L_{dc} can be expressed as:

$$H(s) = \frac{u_{(1)12}(s)}{u_{(1)13}(s)} = \frac{1 - k_1 x}{k_1 x + s\tau_1 x} \cdot \frac{sL_{dc}}{Z_{c(1)}}. \quad (16)$$

To analyze the frequency-magnitude response [21], [24], we have $H(j\omega)$ as:

$$H(j\omega) = \frac{(1 - k_1 x)L_{dc}j\omega}{\tau_1 x Z_{c(1)}j\omega + k_1 x Z_{c(1)}},$$

$$\lim_{\omega \rightarrow \infty} |H(j\omega)| = \frac{(1 - k_1 x)L_{dc}}{\tau_1 x Z_{c(1)}}. \quad (17)$$

The magnitude of the frequency response of $H(j\omega)$ is shown in Fig. 4 for different L_{dc} and fault distance x (where k_1 and τ_1 are constants in equation (17)). The L_{dc} , as a boundary element, filters out high-frequency components in $u_{(1)13}(s)$ which are measured at the external relays, leading to a significant difference in frequency information between $u_{(1)12}(s)$ and $u_{(1)13}(s)$. In light of (17) and Fig. 4, we can draw the conclusion that: 1) The magnitude of $H(j\omega)$ is influenced by the value of L_{dc} in the high-frequency range when $\omega = 2\pi f \rightarrow \infty$. As L_{dc} increases, the amplitude of the high-frequency components in $u_{(1)12}(s)$ increases, whereas the amplitude of $u_{(1)13}(s)$ decreases. Conversely, as L_{dc} decreases, the opposite effect is observed; 2) The fault distance x also impacts $H(j\omega)$ by determining the extent of the attenuation of the TWs propagation process. A smaller value of x results in a higher amplitude of high-frequency components in $u_{(1)12}(s)$ and a lower amplitude in $u_{(1)13}(s)$, while the opposite is observed for a larger value of x ; 3) When the size of L_{dc} is increased, the sensitivity and selectivity performance of the protection will also increase. This is because L_{dc} significantly impacts the transfer function $H(j\omega)$ characteristics and the high-frequency components. In contrast, the opposite is observed for a smaller value of L_{dc} . 4) These characteristics hold for all fault types and other relays as well.

D. Difference of High-Frequency Components in Faulty and Healthy Pole Voltages

According to (9) and Table III, the zero-mode voltage $u_{(0)12}(s)$ can be expressed as:

$$u_{(0)12}(s) = \frac{2\Delta u_{F0}}{s} \left(1 - \frac{Z_{c(0)}}{Z_{c(0)} + sL_{dc}}\right) \frac{1 - k_0 x}{1 + s\tau_0 x} e^{-s\frac{x}{v_{(0)}}}, \quad (18)$$

where $v_{(0)}$ is the propagation velocity of zero-mode TWs in the cable. The values are $k_0 = 7 \times 10^{-5}/\text{km}$, and $\tau_0 = 1.2 \times 10^{-8} \text{ s/km}$ as the zero-mode TWs have smaller velocity and larger attenuation constant.

By applying the mode-to-pole transformation (inverse of (1)), the pole voltages u_{p12} , u_{n12} are:

$$u_{p12} = \frac{u_{(0)12} - u_{(1)12}}{\sqrt{2}}, \quad u_{n12} = \frac{u_{(1)12} + u_{(0)12}}{\sqrt{2}}. \quad (19)$$

By combining (9), (18) and (19) yields that:

$$u_{p12}(s) = \frac{1}{\sqrt{2}} \left(\frac{2\Delta u_{F0}}{s} \frac{sL_{dc}}{Z_{c(0)} + sL_{dc}} \frac{1 - k_0 x}{1 + s\tau_0 x} e^{-s\frac{x}{v_{(0)}}} - \frac{2\Delta u_{F1}}{s} \frac{sL_{dc}}{Z_{c(1)} + sL_{dc}} \frac{1 - k_1 x}{1 + s\tau_1 x} e^{-s\frac{x}{v_{(1)}}} \right),$$

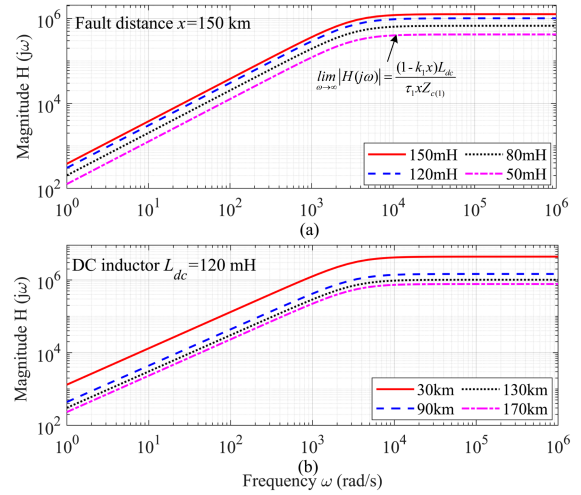


Fig. 4. Magnitude-frequency response of $H(j\omega)$: (a) Impact of DC inductor L_{dc} ; (b) Impact of fault distance x .

$$u_{n12}(s) = \frac{1}{\sqrt{2}} \left(\frac{2\Delta u_{F1}}{s} \frac{sL_{dc}}{Z_{c(1)} + sL_{dc}} \frac{1 - k_1 x}{1 + s\tau_1 x} e^{-s\frac{x}{v_{(1)}}} + \frac{2\Delta u_{F0}}{s} \frac{sL_{dc}}{Z_{c(0)} + sL_{dc}} \frac{1 - k_0 x}{1 + s\tau_0 x} e^{-s\frac{x}{v_{(0)}}} \right). \quad (20)$$

According to Table III and (20), Δu_{F0} is zero in the case of PTP fault. Thus, we have: $u_{p12}(s) = u_{n12}(s) = \frac{1}{\sqrt{2}} u_{(1)12}(s)$. The pole voltages $u_{p12}(s)$ and $u_{n12}(s)$ will drop rapidly when the TWs arrive at R_{12} and present a symmetrical transient behavior. While in the case of PTG or NTG fault, only the faulty pole voltage will decrease to zero instantaneously, whilst the non-faulty pole voltage is marginally damped.

If we neglect the attenuation effect of TWs in (20), we have the transfer function $G_{pn}(s) = u_{p12}(s)/u_{n12}(s)$ as:

$$\lim_{s \rightarrow \infty} |G_{pn}(s)| = \lim_{s \rightarrow \infty} \left| \frac{u_{p12}(s)}{u_{n12}(s)} \right| = \begin{cases} 1, & \text{PTP} \\ \left| \frac{Z_{c(0)} + Z_{c(1)}}{Z_{c(0)} - Z_{c(1)}} \right|, & \text{PTG} \\ \left| \frac{Z_{c(0)} - Z_{c(1)}}{Z_{c(0)} + Z_{c(1)}} \right|, & \text{NTG} \end{cases} \quad (21)$$

where $Z_{c(1)} = 60.714 \Omega$, $Z_{c(0)} = 169.587 \Omega$ in the tested cable. As seen in (21), the magnitude of $|G_{pn}(s)|$ varies depending on the fault types when $s \rightarrow \infty$. The high-frequency components present in the voltages of the faulty pole exhibit a larger amplitude than those of healthy pole.

In light of previous analyses, we conclude that: 1) The faulty area can be discriminated using the high-frequency components contained in line-mode voltages; 2) The fault type can be determined using the high-frequency components contained in pole voltages.

IV. INTRODUCTION OF THE PROPOSED PROTECTION ALGORITHM

This section introduces the proposed protection scheme and the principle of selecting the thresholds.

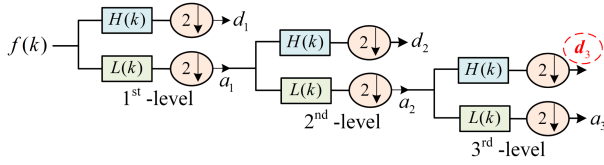


Fig. 5. Schematic Diagram of Mallet Tree of DWT.

A. Step 1: Protection Start-Up Criterion

The protection algorithm is first activated by a start-up criterion. When a DC fault occurs in the system, the DC voltage $V_{dc,ij}$ will drop immediately. Thus, the protection start-up criterion can be established by applying DC under-voltage detection criteria, which can be expressed as:

$$|V_{dc,ij}| = |u_{p,ij} - u_{n,ij}| < V_{dc,Thre} \quad (22)$$

where $V_{dc,Thre}$ denotes threshold for start-up criterion.

B. Step 2: Fault Area Detection Criterion

The fault area detection criterion is based on the maximum absolute value of the high-frequency components contained in the line-mode voltage. In our research, the discrete wavelet transform (DWT) is selected as a signal processing tool, chiefly due to its high computational speed and data compression capability for signal edge detection. For a given discrete signal $f(k)$, the DWT algorithm can be obtained as,

$$DWT(f, m, n) = \frac{1}{\sqrt{a_0^m}} \sum_k f(k) \Psi^* \left(\frac{n - kb_0 a_0^m}{a_0^m} \right) \quad (23)$$

where the scale parameter and translation parameter are a_0^m and $kb_0 a_0^m$. In this work, they are adopted as $a_0 = 2$ and $b_0 = 1$, respectively.

The actual implementation of the DWT is achieved by using the Dyadic Mallet Tree algorithm, which is depicted in Fig. 5. The signal $f(k)$ is repeatedly decomposed by cascaded high- and low-pass filters ($H(k)$ and $L(k)$). To enhance the frequency resolution and ensure the time localization of each scaled level, the results after both high- and low-pass filters are down-sampled with a factor of two.

The Haar wavelet is selected as the mother wavelet due to the following benefits [26] compared to other mother wavelets (e.g., ‘Daubechies’, ‘Symlets’, and ‘Coiflets’): 1) The Haar wavelet is a simple piecewise constant wavelet, making it a preferred choice for real-time applications where computational efficiency and easy implementation is required; 2) It shows good properties for edge detection, as it can detect changes in the signal that occur over time.

The choice of the data decomposition level is a trade-off between the frequency resolution of decomposed detailed coefficients and the robustness of protection algorithm against noise interference. Considering that the high-pass filters will add a time advance for the processed data, the higher level (e.g. 4th, 5th) decomposed detailed coefficients fail to represent the accurate TW arriving time. In addition, the waveforms of these

high-level decomposed coefficients are close to the stepped signals presenting low-resolution problems, which are not suitable for protection design. The lower-level (e.g. 1st, 2nd) decomposed detailed coefficients require high-sampling frequency for measurements and are sensitive to the noise intervention. To this end, the proposed algorithm utilizes the 3rd scale detailed coefficients for the fault detection. In our research, the sampling frequency of the DWT is set to 100 kHz. This is because a low sampling frequency reduces the resolution of high-frequency components and increases the time delay introduced by DWT, which ultimately impacts the performance of the protection scheme in terms of speed, sensitivity, and selectivity.

The high-frequency components of each decomposed line-mode voltage are denoted as $d_3 u_{(1)ij}$ ($i, j = 1, 2, 3, 4$). The detailed criterion to identify the faulty area can be expressed as follows:

$$|d_3 u_{(1)ij}| > d_3 u_{(1)ij,Thre} \quad (24)$$

where $d_3 u_{(1)ij,Thre}$ denotes the threshold for fault area detection criterion.

C. Step 3: Fault Type Identification Criterion

The DWT is also utilized to extract the high-frequency components $d_3 u_{p,ij}$ and $d_3 u_{n,ij}$ contained in the pole voltages. To discriminate the specific fault type, the wavelet energy difference ΔE_{ij} between positive and negative poles is calculated by:

$$Ed_3 u_{pn,ij} = \sum_{k=1}^{K=10} (d_3 u_{pn,ij}(k))^2$$

$$\Delta E_{ij} = |Ed_3 u_{p,ij}| - |Ed_3 u_{n,ij}| \quad (25)$$

where $Ed_3 u_{p,ij}$ and $Ed_3 u_{n,ij}$ denote the wavelet energy of positive and negative pole voltage components in cable ij .

The selection of K is a trade-off between the detection speed and accuracy. If K is too large, it will reduce the detection speed, and bring a huge computation burden. If K is too small, the processing of high-frequency signals is not accurate enough, it easily affects the protection selectivity and reliability, and the robustness of protection of withstanding noise intervention is also reduced. Considering a certain level of tolerance, K is set to 10 in our study.

Then, we obtain the fault type identification criterion as:

$$\begin{cases} \Delta E_{ij} \geq \Delta E_{set1}(PTG), \Delta E_{ij} \leq \Delta E_{set2}(NTG) \\ \Delta E_{set2} \leq \Delta E_{ij} \leq \Delta E_{set1}(PTP) \end{cases} \quad (26)$$

where ΔE_{set1} and ΔE_{set2} are the thresholds for fault type identification. Due to the symmetrical system configuration, the ΔE_{ij} presents the same magnitude and opposite polarity under PTG and NTG faults. Thus, the ΔE_{set2} is set as $-\Delta E_{set1}$ in our work.

D. Determination of Threshold Values

1) *Step 1:* The selection of $V_{dc,Thre}$ is a trade-off between the robustness to noise interference and the sensitivity against HIF. If $V_{dc,Thre}$ is set above 0.95 p.u., the relay units could be

activated by noise interference of 25 dB, which would impact the performance of subsequent steps. On the other hand, if the $V_{dc,Thre}$ is set below 0.95 p.u., the relay units may not detect internal HIF. After numerous simulation studies, the choice of 0.95 p.u. of $V_{dc,Thre}$ could guarantee that the protection could be activated correctly under internal HIF (Considering R_f up to 500 Ω) and 25 dB noise interference.

2) *Steps 2 and 3:* The selection of the thresholds of step 2 must ensure successful selectivity and sensitivity of the protection. Specifically, the $d_3u_{(1)ij,Thre}$ should be greater than the maximum absolute value of $d_3u_{(1)ij}$ under the most serious external fault, and be smaller than the minimum absolute value of $d_3u_{(1)ij}$ for an internal HIF, assuming $R_f \leq 500 \Omega$. The $d_3u_{(1)ij,Thre}$ must satisfy the following condition:

$$k_{sen} \min |d_3u_{(1)ijin}| > d_3u_{(1)ij,Thre} > k_{rel} \max |d_3u_{(1)ijex}| \quad (27)$$

where $d_3u_{(1)ijex}$ is the d_3 component when the most serious external fault occurs, which is generally considered as a metallic PTP fault occurring at the outlet of a neighboring cable [27]. $d_3u_{(1)ijin}$ is the d_3 component when an internal fault ($R_f = 500 \Omega$) occurs on cable ij . Therefore, when (24) is met, it is considered that an internal fault has occurred. Otherwise, it is understood as an external fault.

For the studied relays R_{12} and R_{21} , the most serious external fault is the metallic PTP fault occurring at the outlet of cable13 and cable24, respectively. Based on the simulations results, the largest value of $d_3u_{(1)12ex}$ under external fault f_{13} is 0.6368, $d_3u_{(1)21ex}$ under external fault f_{24} is 1.2733; Furthermore, the smallest value of $d_3u_{(1)12in}$ and $d_3u_{(1)21in}$ under internal HIF ($R_f = 500 \Omega$) is 1.65 and 2.17, respectively. In this study, we consider a reliability coefficient of $k_{rel} = 1.2$ [27], and a sensitivity coefficient of $k_{sen} = 0.85$. According to (27), the thresholds should satisfy: $d_3u_{(1)12,Thre} \in (0.764, 1.403)$ and $d_3u_{(1)21,Thre} \in (1.527, 1.84)$. To accelerate the detection speed, finally $d_3u_{(1)12,Thre} = 0.764$ and $d_3u_{(1)21,Thre} = 1.527$. In this way, both the selectivity and sensitivity of step 2 are guaranteed. The thresholds of other relays should be selected in the same way.

The determination of the thresholds ΔE_{set1} and ΔE_{set2} mainly considers the internal HIF, as selectivity is already guaranteed by step 2. Following the threshold determination procedures for step 2, we set ΔE_{set1} and ΔE_{set2} are set to 23.10 and -23.10 for R_{12} , and set to 93.5 and -93.5 for R_{21} respectively.

E. Protection Algorithm Working Steps

The flow chart of the proposed protection scheme is depicted in the following Fig. 6. The scheme consists of three steps. To begin with, the DC voltage $V_{dc,ij}$ is sampled to determine whether the start-up criteria are met or not. If they are satisfied, the algorithm moves to the next step that identifies the faulty area using the $d_3u_{(1)ij}$ as illustrated in (24). Once an internal fault is determined, the wavelet energy difference ΔE_{ij} is adopted to identify the specific fault type as explained in (25), the interruption commands will be tripped to the corresponding

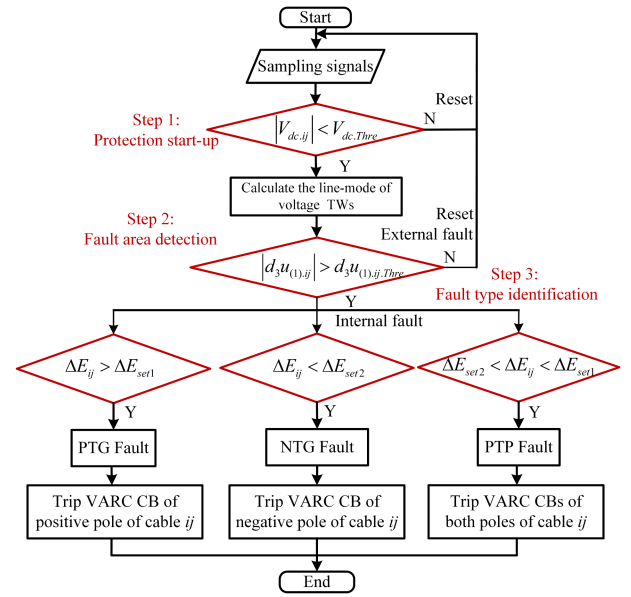


Fig. 6. Flowchart of overall protection scheme.

VARC DCCB, the model of which is applied to demonstrate fault current interruption. Otherwise, the protection will be reset.

To implement the proposed protection to other test systems, it is necessary to determine suitable protection threshold values according to the aforementioned steps. For its practical application, the proposed work can be programmed in hardware Field Programmable Gate Array (FPGAs) units using e.g., Virtex, Xilinx, Altera Quartus by VHDL language. The programmed FPGAs units act as protective relays and can be tested in a control hardware-in-the-loop with the cyber-physical real-time digital simulator (RTDS). The communications can be established via open-source Aurora protocol and IEC 61850-9-2 standard.

V. SIMULATION AND RESULTS ANALYSIS

A. Performance Under Internal Fault Cases

1) *Protection Start-Up:* For the observed relay units R_{12} and R_{21} , fault scenarios on cable12 are internal DC faults. All test faults are applied at 1.2 s on cable12 with various fault distances x , the fault-impedance R_f is varied from 0.1 Ω to 500 Ω . The sampling rate of 100 kHz in PSCAD/EMTDC was chosen for the protection algorithm to capture the features of high-frequency components using wavelet transform, which is technically possible to achieve in practice. Typical commercially available high-resolution relays are SEL-T401 L, SEL-T400 L, and SEL-TWFL.

Fig. 7 presents the results of the protection start-up criteria against fault $f_{12}|PTP(x = 50 \text{ km})$. The fault distance from the relay R_{12} is 50 km. When the voltage TW arrives at R_{12} , the voltage V_{dc12} drops less than the threshold of 0.95 p.u. within 0.3 ms. Similarly, the voltage V_{dc21} starts to decrease later since the fault distance x for R_{21} is 150 km. It is visible that the start-up process is affected by the fault resistance, which impacts the TW propagation by changing the wave impedance

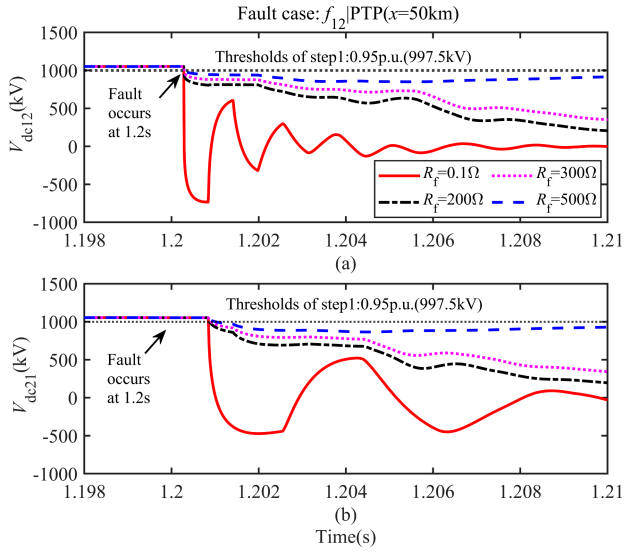


Fig. 7. Simulation of DC voltage with $f_{12}|PTP(x = 50 \text{ km})$. (a) DC voltage V_{dc12} . (b) DC voltage V_{dc21} .

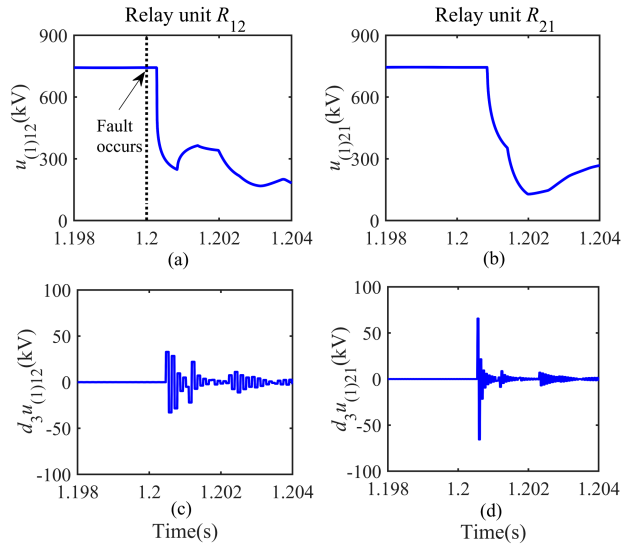


Fig. 8. Simulation of fault scenario: $f_{12}|PTP(x = 50 \text{ km}, R_f = 50 \Omega)$.

alongside the faulty cable. The protection operation threshold is 0.95 p.u. (997.5 kV), and it can be satisfied with R_f up to 500 Ω , which confirms desired sensitivity performance of the protection scheme to HIF.

2) *Fault Area Identification*: Fig. 8 presents the line-mode voltage $u_{(1)12}$ and $u_{(1)21}$ and their corresponding d_3 components. According to Fig. 8(a) and (b), the line-mode voltage TWs measured at R_{12} and R_{21} are constant values in steady-state. When the fault occurs at 1.2 s, the attenuation and oscillation at the initial post-fault stage of $u_{(1)12}$ and $u_{(1)21}$ occur, and are accompanied by the refraction and reflection of the line-mode voltage TW. Fig. 8(c) and (d) demonstrate the appearance of the d_3 components. The magnitude depends on the specific fault distance x , and the fault-resistance R_f . At steady- and post-fault states, the amplitudes of $d_3u_{(1)12}$ and $d_3u_{(1)21}$ are close to zero.

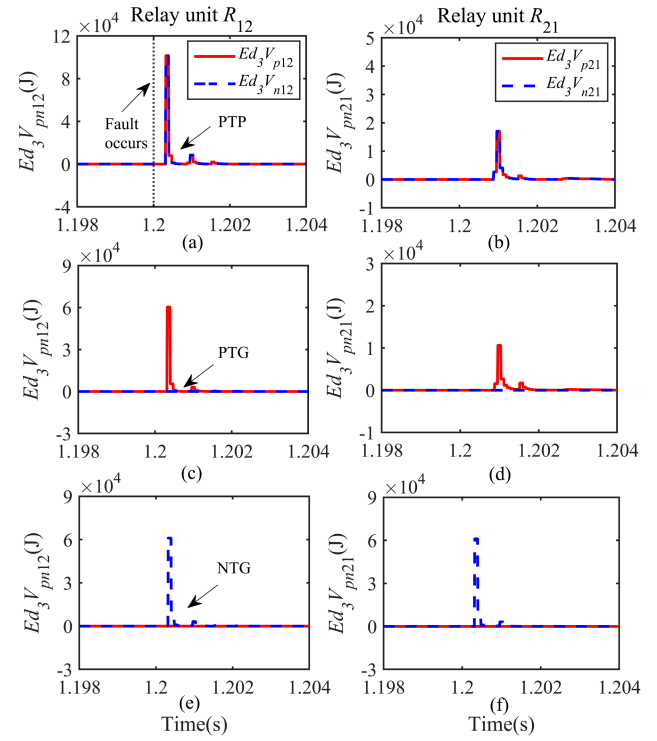


Fig. 9. Simulation of wavelet energy of positive and negative poles.

The maximum transient values can be extracted at the instant when the line-mode TW arrives at the relay units. The protection thresholds are then satisfied and start to identify the specific fault type.

3) *Fault Type Identification*: Fig. 9 presents the energy difference measured at the relay units R_{12} and R_{21} for faults scenarios $f_{12}|PTP(x = 50 \text{ km})$, $f_{12}|PTG(x = 50 \text{ km})$ and $f_{12}|NTG(x = 50 \text{ km})$, respectively. The fault resistance is set at 10 Ω . From Fig. 9(a) and (b), it can be seen that when the TW arrives at the cable terminals, the wavelet energy of d_3u_{p12} and d_3u_{n12} at both poles will increase instantly to a distinguishable value. Since the fault type is a PTP fault, the transient behavior of the positive and negative poles presents a symmetrical trend. The wavelet energy is nearly the same. Thus, the energy difference in accordance to (24) is close to zero. However, the wavelet energy can solely be located at the positive pole as proven in Fig. 9(c) and (d) in the case of PTG fault, whilst the wavelet energy of the negative pole is close to zero. Similar results are also found for NTG fault as illustrated in Fig. 9(e) and (f). By using this feature, the fault type is then determined by (26). The test results for more internal fault scenarios are shown in Table IV through Table VI. All signals $d_3u_{(1)12}$ and $d_3u_{(1)21}$ monitored at R_{12} and R_{21} exceed the threshold value for any fault condition. By taking the energy difference ΔE_{12} and ΔE_{21} in the case of PTP fault as an example, it can be seen that the computed maximum energy difference (which in this case is 19.14) is relatively small. However, the magnitude of the energy difference in the case of a PTG or a NTG fault is much greater than that of a PTP fault. It is noted that the polarity of the energy difference for a PTG and a NTG fault is opposite due to the energy definition in (25);

TABLE IV
TEST RESULTS UNDER FAULT: $f_{12}|PTP(x = 50 \text{ km})$

Fault Case	Relay Unit R_{12}			Relay Unit R_{21}			
	R_f (Ω)	$d_3u_{(1)12}$ (kV)	ΔE_{12} (kV)	Trip (ms)	$d_3u_{(1)21}$ (kV)	ΔE_{21} (kV)	Trip (ms)
0	376.44	19.14	PN/0.30	200.57	9.11	PN/0.86	
10	267.44	9.87	PN/0.60	142.44	0.13	PN/0.88	
50	32.79	0.40	PN/0.48	65.61	0.07	PN/0.87	
100	19.59	0.23	PN/0.48	39.18	0.04	PN/0.88	
200	10.83	0.13	PN/0.48	21.70	0.02	PN/0.89	
300	7.49	0.087	PN/0.48	15.0	0.023	PN/0.92	
500	4.63	9.052	PN/0.48	9.27	0.007	PN/1.03	

TABLE V
TEST RESULTS UNDER FAULT: $f_{12}|PTG(x = 100 \text{ km})$

Fault Case	Relay Unit R_{12}			Relay Unit R_{21}			
	R_f (Ω)	$d_3u_{(1)12}$ (kV)	ΔE_{12} (kV)	Trip (ms)	$d_3u_{(1)21}$ (kV)	ΔE_{21} (kV)	Trip (ms)
0	101.33	2.77e5	P/0.58	117.33	2.77e5	P/0.58	
10	56.53	8.78e4	P/0.58	66.23	8.78e4	P/0.58	
50	20.28	1.15e4	P/0.58	23.93	1.15e4	P/0.58	
100	11.26	3.54e3	P/0.58	13.31	3.54e3	P/0.58	
200	5.96	990.52	P/0.59	7.05	990.4	P/0.59	
300	4.05	460.03	P/0.59	4.79	450.94	P/0.59	
500	2.47	170.12	P/0.64	2.93	170.07	P/0.65	

TABLE VI
TEST RESULTS UNDER FAULT: $f_{12}|NTG(x = 150 \text{ km})$

Fault Case	Relay Unit R_{12}			Relay Unit R_{21}			
	R_f (Ω)	$d_3u_{(1)12}$ (kV)	ΔE_{12} (kV)	Trip (ms)	$d_3u_{(1)21}$ (kV)	ΔE_{21} (kV)	Trip (ms)
0	110.64	-31.e8	N/0.86	39.46	-200.6e3	N/0.30	
10	62.4	-10.76e3	N/0.87	23.17	-61.1e3	N/0.30	
50	22.59	-1.5e3	N/0.87	8.66	-7.73e3	N/0.32	
100	12.57	-0.47e3	N/0.98	4.86	-2.37e3	N/0.30	
200	6.67	-0.13e3	N/1.45	2.59	-660.25	N/0.44	
300	4.54	-60.14	N/1.45	1.76	-300.59	N/0.46	
500	2.77	-30.32	N/1.45	1.57	-110.36	N/0.62	

Therefore, the PTG and the NTG fault is discriminated. It can be concluded that all faulty areas can be detected, and all fault types can be identified. The relay units R_{12} and R_{21} operate correctly by sending tripping signals to the corresponding VARC DCCBs within 2 ms.

B. Performance Under External Fault

Several external fault scenarios are carried out on external zones of cable12. Detailed results are summarized in Table VII. Regarding these external faults, the magnitudes of $d_3u_{(1)12}$ and $d_3u_{(1)21}$ for any external fault are lower than the thresholds. The maximum magnitudes of $d_3u_{(1)12}$ and $d_3u_{(1)21}$ are 0.6368 and 1.2733, respectively. However, compared to the results of the internal DC faults listed in Tables IV to VI, the magnitudes of $d_3u_{(1)12}$ and $d_3u_{(1)21}$ are relatively small. The protection will be then reset.

TABLE VII
RESULTS OF THE PROTECTION AGAINST EXTERNAL FAULTS

External Faults ($x(\text{km}), R_f(\Omega)$)	$ d_3u_{(1)12} $ (kV)	$ d_3u_{(1)21} $ (kV)	Step2 Met?
$f_1 (\text{DC bus1 fault})$	0.3918	0.3149	×
$f_2 (\text{DC bus2 fault})$	0.5049	0.5520	×
$f_3 (\text{DC bus4 fault})$	0.0251	0.0866	×
$f_4 (\text{AC grid1 fault})$	0.0453	0.0391	×
$f_5 (\text{AC grid2 fault})$	0.0634	0.0526	×
$f_{13} PTG(x = 0, R_f = 0)$	0.3291	0.3292	×
$f_{13} PTP(x = 0, R_f = 0)$	0.6368	0.4175	×
$f_{24} PTP(x = 0, R_f = 0)$	0.3636	1.2733	×
$f_{13} PTP(x = 0, R_f = 10)$	0.5679	1.1365	×
$f_{13} PTP(x = 0, R_f = 50)$	0.3774	0.7580	×
$f_{13} PTG(x = 100, R_f = 0)$	0.0884	0.1190	×
$f_{24} PTG(x = 100, R_f = 0)$	0.1728	0.1233	×
$f_{34} PTP(x = 100, R_f = 0)$	0.0180	0.0342	×
$f_{34} PTG(x = 100, R_f = 0)$	0.0060	0.0165	×

C. Tripping Time Delay Evaluation

The tripping time t_{trip} of the protection in Fig. 6 is comprehensively determined, and computed as follows:

$$t_{trip} = \frac{x}{v_{(1)}} + t_{step1} + 50 \mu\text{s} + t_{step2} + 50 \mu\text{s} + t_{step3}. \quad (28)$$

In (28), $50 \mu\text{s}$ is the sensor's time delay between each step. $x/v_{(1)}$ represents the TWs propagation delay. Based on the given values, the calculation of $x/v_{(1)}$ yields a result that: $x/v_{(1)} \leq 1.107 \text{ ms}$. This calculation is based on a maximum possible fault distance of $x = 200 \text{ km}$ for cable 12, and the velocity for $v_{(1)} = 1.806 \times 10^5 \text{ km/s}$.

The value of t_{step1} in (22) is influenced by the R_f and the fault type. When an NTG or PTG fault occurs with a fault resistance of $R_f = 500 \Omega$, it is observed that $t_{step1} \leq 0.52 \text{ ms}$. In general, a higher value of R_f results in a larger value of t_{step1} . t_{step2} is mainly determined by the time delay caused by the use of DWT, which is dependent on three factors: the required decomposition level (3rd-level), the sampling frequency (100 kHz), and the mother wavelet ('Haar'). In the present work, the resulting time delay is 0.05 ms.

Once criterion (22) is satisfied, the measured $d_3u_{(1)ij}$ will exceed the corresponding thresholds after a few sampling intervals ($10 \mu\text{s}$ for one sample). t_{step3} is determined by the time delay of DWT, and the computational delay of the energy calculator in (25). Recall $K = 10$ in (25), the time interval for calculating one data ΔE_{ij} in (25) is $10 \times 10 \mu\text{s} = 0.1 \text{ ms}$. The measured ΔE_{ij} meets (26) within a few time intervals.

Taking the relay R_{12} as an example, the longest tripping time t_{trip} for the fault $f_{12}|PTG(x = 200 \text{ km}, R_f = 500 \Omega)$ is 1.747 ms. Consequently, the proposed protection meets the requirements of fault detection speed for practical HVDC applications.

D. Interaction Between Protection and VARC DCCBs for Fault Current Interruption

Fig. 10 presents a successful fault current interruption by the VARC DCCB based on protection operation for a fault scenario:

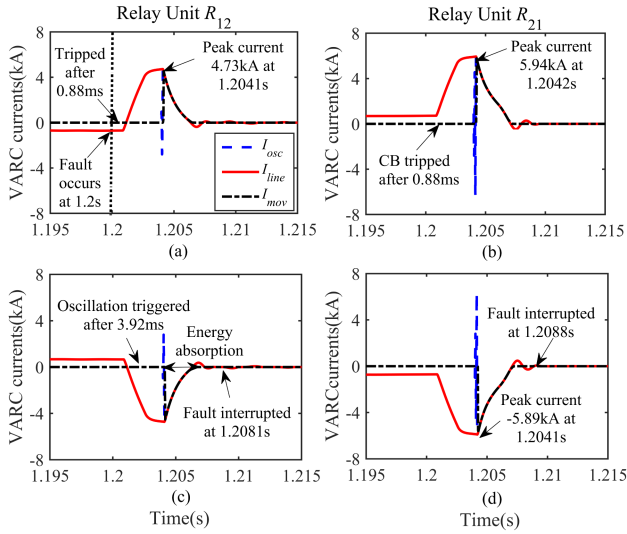


Fig. 10. Simulation of VARC DCCB Currents. (a). Positive pole at R_{12} . (b). Positive pole at R_{21} . (c). Negative pole at R_{12} . (d). Negative pole at R_{21} .

TABLE VIII
NOISE TEST RESULTS WITH A DIFFERENT NOISE LEVEL AND A FAULT
RESISTANCE $R_f(\Omega)$

$f_{12} PTG$ ($x = 100\text{km}$)	SNR=25 dB			SNR=40 dB		
	0 Ω	100 Ω	200 Ω	0 Ω	100 Ω	200 Ω
$\max d_3u_{(1)12} $	72.46	29.17	35.20	92.55	6.84	8.45
ΔE_{12}	1.4e5	2.2e3	2.9e3	1.3e5	1.7e3	1.67e3
Tripping	✓ P	✓ P	✓ P	✓ P	✓ P	✓ P
$f_{12} NTG$ ($x = 150\text{km}$)	SNR=25 dB			SNR=40 dB		
	0 Ω	100 Ω	200 Ω	0 Ω	100 Ω	200 Ω
$\max d_3u_{(1)12} $	30.13	23.44	26.16	40.12	5.42	6.16
ΔE_{12}	-2.8e4	-2.3e3	-3.2e3	-3.3e4	-428.1	-120.2
Tripping	✓ N	✓ N	✓ N	✓ N	✓ N	✓ N

$f_{12}|PTP(x = 100\text{ km}, R_f = 0\ \Omega)$. The I_{osc} , I_{line} , and I_{mov} refer to the oscillating current, cable current, and current in the surge arrester branch [22], respectively. In this fault scenario, the VARC DCCB is activated at 1.2088 s. For the VARC DCCB in R_{12} , it is observed that it starts generating the oscillating current I_{osc} at 3.92 ms after the fault occurrence. The peak fault currents are 4.73 kA and -4.73 kA at 1.2041 s. Then, the fault currents are interrupted by the main vacuum interrupter at 1.2081 s. The peak fault currents in the VARC DCCB are 5.94 kA and -5.94 kA, respectively. The fault currents are interrupted at 1.2088 s. The VARC DCCBs installed in other cables are not activated. Fig. 10 reveals that the proposed protection scheme and the DCCBs have good interaction performance. The observed faulty area and the fault type is discriminated correctly, the corresponding faulty poles of cable12 can be interrupted promptly.

E. Influence of Noise on Protection Performance

The Gaussian White Noises (GWN) are added to the sampled TW signals with different signal-noise-ratio (SNR) levels: 25 dB and 40 dB. Two independent fault cases are performed in the studied system, and the test results at the relay unit R_{12} are presented in Table VIII. The step1 of the protection is minimally affected by the noise, and the relay units can be activated

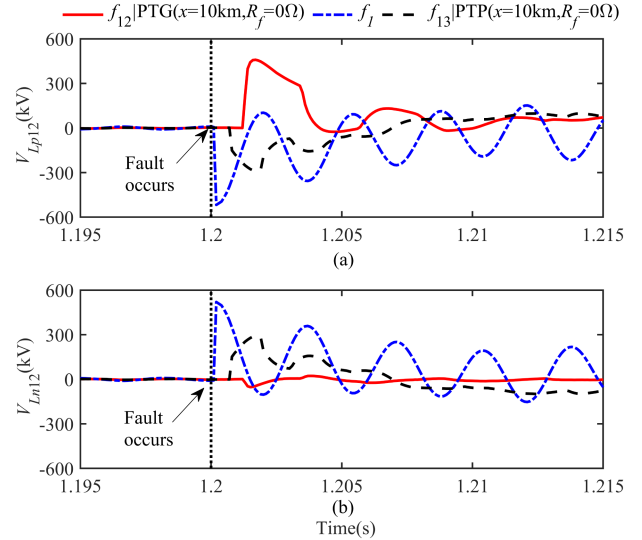


Fig. 11. DC inductor voltages. (a). V_{Lp12} at positive pole. (b). V_{Ln12} at negative pole.

correctly with noise interference. Since the white noises can be regarded as high-frequency harmonics to line-mode voltage, the magnitude of $d_3u_{(1)12}$ and ΔE_{12} are affected proportionally to the level of the noise intervention as shown in Table VIII. However, the maximum absolute values of $d_3u_{(1)12}$, and energy difference ΔE_{12} exceed the selected thresholds for the faulty area and the fault type identification. Therefore, the results confirm that the proposed protection scheme is sufficiently robust to withstand the 25 dB noise intervention.

F. Comparison With Other Methods

1) *Comparison With a DC Inductor Voltage Changed Rate Based Method:* A DC inductor voltage change rate based protection scheme is proposed in [9]. For comparison purposes, the fault location indication time is set to 180 μs , the predefined thresholds of V_{LTt1} and V_{LTt2} are set as 5 kV and 10 kV, which are in line with the values in [9]. Three independent faults are simulated to verify algorithm effectiveness. The simulation of the inductor voltages V_{Lp12} and V_{Ln12} at cable12 terminal are shown in Fig. 11.

The voltages across the inductors increase rapidly after the fault occurrence. Following the fault $f_{12}|PTG(x = 10\text{ km})$, the protection method in [9] operates correctly. However, it is seen that the inductor voltages also surge during the external fault $f_{13}|PTP(x = 10\text{ km}, R_f = 0\ \Omega)$ and the bus fault f_1 ; Furthermore, they experience similar trends at the fault initial stage with the fault $f_{12}|PTG(x = 10\text{ km}, R_f = 0\ \Omega)$. The thresholds of 5 kV and 10 kV are promptly exceeded. The protection will malfunction and trip both DCCBs at R_{12} , resulting in taking out the healthy cable of service. In contrast, the proposed algorithm, will correctly identify internal and external faults for cable12 as validated in previous subsections. Thus, the protection method in [9] presents low selectivity. In addition, the procedures of thresholds selection in [9] are complicated to be applied in other systems or industrial projects. The time window Δt between

TABLE IX
MAD BASED TWP PERFORMANCE WITH DIFFERENT $R_f(\Omega)$

F1	Item (p.u.)	10 Ω	50 Ω	100 Ω	200 Ω
MAD	I_{dc12+}	8.276	4.351	2.574	1.619
	I_{dc12-}	9.320	5.793	2.644	1.509
	I_{dc21+}	9.081	5.785	4.277	3.157
	I_{dc21-}	9.023	5.704	4.177	3.050
	V_{dc12+}	-0.501	-0.272	-0.171	-0.098
MAD_M	V_{dc12-}	-0.50	-0.272	-0.171	-0.098
	V_{dc21+}	-0.422	-0.198	-0.122	-0.069
	V_{dc21-}	-0.422	-0.197	-0.123	-0.068
F1 Trip	$R_{12}\&R_{21}$	\sqrt{PN}	\times	\times	\times
F2	Item (p.u.)	10 Ω	50 Ω	100 Ω	200 Ω
MAD	I_{dc12+}	8.828	4.118	2.077	1.612
	I_{dc12-}	8.875	4.180	2.151	1.498
	I_{dc21+}	11.278	6.812	4.895	3.493
	I_{dc21-}	11.249	6.736	4.803	3.389
	V_{dc12+}	-0.478	-0.249	-0.155	-0.086
MAD_M	V_{dc12-}	-0.479	-0.249	-0.156	-0.087
	V_{dc21+}	-0.478	-0.249	-0.154	-0.085
	V_{dc21-}	-0.478	-0.249	-0.154	-0.085
F2 Trip	$R_{12}\&R_{21}$	\sqrt{PN}	\times	\times	\times

two thresholds (inductor voltage increase from 5 kV to 10 kV) requires precise signal measuring, which makes the protection susceptible to noise intervention.

2) *Comparison With Median Absolute Deviation (MAD) Based Transient Signal Detection*: A MAD-based TWP is proposed in [28], which realizes the fault detection by locating the outliers in the sampling dataset of voltage and current TWs. A faulty pole is detected if the criteria $W_{MAD}(t) \geq \Delta_1$ and $W_{MAD_M}(t) \leq \Delta_2$ are satisfied. Here $W_{MAD}(t)$ and $W_{MAD_M}(t)$ refer to the results processed by MAD, and the modified MAD algorithm MAD_M from the sampling current and voltage TWs, respectively. The thresholds Δ_1 and Δ_2 are set as 6.0 p.u. and -0.2 p.u., respectively. The latest 50 samples are considered, which is in line with the design in [28]. Two fault cases in [28] are also investigated for the studied system:

- F1: PTP fault on cable12 50 km from bus C1.
- F2: PTP fault on cable12 100 km from bus C1.

The data calculated at the relay units R_{12} and R_{21} of cable12 are summarized in Table IX. The magnitudes of MAD.I and MAD.V are inversely proportional to the fault impedance. The results for the positive and negative poles are very close due to the symmetrical fault and system configuration. When the fault-impedance exceeds 50 Ω , the damping of the voltage and current TWs is not obvious, and the criterion in [28] is not satisfied. Thus, the MAD fails to extract the outliers from the sampling dataset (marked as red). This confirms the limit of the sensitivity of MAD-based TW protection, whilst the proposed protection scheme is capable of detecting high-impedance (up to 500 Ω) correctly. Furthermore, the MAD-based protection is not robust enough to withstand the noise intervention as it will regard the noises as outliers, whilst the proposed method is demonstrated to operate correctly with a 25 dB noise intervention.

3) *Comparison With Commercially Available Methods*: The TWP in [27] uses voltage/current and their derivatives to detect

TABLE X
THE PERFORMANCE OF TWP METHODS IN [8], [27]

Relay R_{12}	F1	F2	F3	F4	F5	F6
$\frac{du_{p12}}{dt}$ (kV/ms)	54012.1	22015.5	5512.3	3066.8	2.21	573.09
Δu_{p12} (kV)	893.69	818.52	114.12	1.373	1.312	630.30
$\frac{du_{n12}}{dt}$ (kV/ms)	54011.9	22015.5	1.963	113.72	3084.5	575.79
Δu_{n12} (kV)	890.38	815.36	3.865	3.399	111.94	631.12
$\frac{di_{p12}}{dt}$ (kA/ms)	3.67	3.154	0.351	0.368	0.042	1.102
Δi_{p12} (kA)	4.79	4.42	0.805	0.726	0.058	2.793
$\frac{di_{n12}}{dt}$ (kA/ms)	3.669	3.149	1.963	0.039	0.365	1.109
Δi_{n12} (kA)	4.776	4.409	0.051	0.042	0.714	2.805
Trips	\sqrt{PN}	\sqrt{PN}	\times	\times	\times	\times
Relay R_{12}	F1	F2	F3	F4	F5	F6
$\frac{dP_{p12}}{dt}$ (kV/ms)	54145.1	22056.4	5520.7	3074.9	2.715	517.76
ΔP_{p12} (kV)	1008.4	1010.04	160.99	155.8	1.693	437.71
$\frac{dP_{n12}}{dt}$ (kV/ms)	53878.9	21974.9	6.213	3.335	5823.89	646.69
ΔP_{n12} (kV)	817.74	712.16	4.510	3.541	121.93	748.88
$\frac{dG_{12}}{dt}$ (kV/ms)	590.61	507.16	2766.1	1545.2	1530.6	697.37
ΔG_{12} (kV)	768.22	708.84	125.10	117.60	24.146	589.44
Trips	\sqrt{PN}	\sqrt{PN}	\times	\times	\times	\times

the faults, which can be expressed as,

$$\begin{cases} \frac{du}{dt} > \Delta set_1 \\ \Delta u > \Delta set_2 \end{cases}, \quad \begin{cases} \frac{di}{dt} > \Delta set_3 \text{ (Rectifier side)} \\ \Delta i > \Delta set_4 \text{ (Inverter side)} \end{cases} \quad (29)$$

where Δset_i ($i = 1, 2, 3, 4$) are thresholds for fault detection.

The TWP in [8] adopts pole-mode wave P_{wave} and ground-mode G_{wave} and their derivatives for fault detection, which can be represented by:

$$\begin{cases} \frac{dP_{wave}}{dt} > \Delta set_1 \\ \Delta P_{wave} > \Delta set_2 \end{cases}, \quad \begin{cases} \frac{dG_{wave}}{dt} > \Delta set_3 \\ \Delta G_{wave} > \Delta set_4 \end{cases} \quad (30)$$

Following the threshold setting procedures in [8], [27], the thresholds Δset_i ($i = 1, 2, 3, 4$) of TWP in [27] in our system are set as 690.94 kV/ms, 757.34 kV, 1.33 kA/ms, and 3.37 kA, respectively. For the TWP criteria in [8], the thresholds are set as 776.02 kV/ms, 898.65 kV, 836.84 kV, and 707.32 kV, respectively. In addition to F1 and F2, the TWP methods in [8], [27] are tested by more fault cases:

- F3: PTG fault 0 km from bus C1 ($R_f = 200 \Omega$)
- F4: PTG fault 50 km from bus C1 ($R_f = 200 \Omega$)
- F5: NTG fault 50 km from bus C1 ($R_f = 200 \Omega$)
- F6: Metallic PTP fault. 0 km at cable13.

It is noted that F1 and F2 are metallic faults. Test results for R_{12} are listed in Table X, both algorithms in [8], [27] could operate correctly under metallic faults F1 and F2. However, the algorithm in [8], [27] fail to trip the DCCBs due to a limited voltage drop and limited current increase during HIF. Thus, the low sensitivity problems are visible in [8], [27] in case of HIF.

4) *Comparison With ROCOV Based Method*: The protection in [5] uses the measured ROCOV to detect faults. Taking the relay units R_{12} and R_{21} as examples, the observed ROCOV at the line side of the di/dt inductor for different faults are summarized in the following Table XI.

TABLE XI
PERFORMANCE OF ROCOV BASED-METHOD [5]

Faults	ROCOV (kV/ms) (Normal)		ROCOV (kV/ms) (SNR=25 dB)		ROCOV (kV/ms) (SNR=40 dB)	
	R_{12}	R_{21}	R_{12}	R_{21}	R_{12}	R_{21}
F1	1.08e3	0.21e3	1.10e3	0.24e3	1.07e3	0.22e3
F2	0.44e3	0.44e3	0.47e3	0.42e3	0.44e3	0.44e3
F3	0.055e3	0.0063e3	0.23e3	0.26e3	0.046e3	0.045e3
F4	0.031e3	0.0061e3	0.27e3	0.25e3	0.044e3	0.044e3
F5	0.031e3	0.0062e3	0.27e3	0.27e3	0.039e3	0.043e3
F6	0.0015e3	0.0014e3	0.18e3	0.18e3	0.029e3	0.036e3

It is obvious that the magnitude of the measured ROCOV for an external fault F6 is even higher than that of internal faults on cable12 when noise interference is present. These results imply that reliability and selectivity performance are vulnerable to noise. Furthermore, [21] has demonstrated that the ROCOV method in [5] is inadequate for identifying HIF faults based solely on the ROCOV criterion as a primary protection criterion. In addition, the ROCOV method in [5] cannot distinguish specific DC fault types.

VI. CONCLUSION

DC transmission line protection is crucial for developing future large-scale MMC-based MTDC systems. By applying the traveling wave theory, high-frequency components contained in the line mode and pole voltages are used for the protection algorithm in this work. The developed protection algorithm comprises three steps: 1) The protection is activated when the DC voltage drops below 0.95 p.u., 2) The faulty area detection is identified using the d_3 components of the line-mode voltage TWs, and 3) The specific fault type is identified by the comparison of the wavelet energy of d_3 components of the pole voltages. The DWT with the 'haar' mother wavelet is the applied signal processing tool. The setting principle of the protection threshold values for the studied and other systems is also elaborated. Finally, the robustness of the proposed protection algorithm is validated on a four-terminal MMC-HVDC system in PSCAD/EMTDC environment.

Based on the simulation results, we determine the robustness of the proposed protection algorithm for testing MTDC grids according to four aspects: 1) Speed: The fast detection and tripping (within 2 ms) of the proposed protection method meets the practical expectations; 2) Selectivity: The protection correctly operates on all internal faults and does not operate on external faults such as AC, DC bus, and neighboring line faults; 3) Sensitivity: The protection successfully discriminates different fault types and detects faults with a resistance of up to 500 Ω ; 4) Reliability: The protection operates correctly under external faults and noise interference (25 dB).

The interaction between the proposed protection algorithm and the VARC DCCBs for fault current interruption is also demonstrated. Due to the prompt fault clearance, the MMCs and the AC grids are minimally affected by the faults. The authors also thoroughly compared the proposed protection algorithm with the DC reactor voltage change rate-based protection, the ROCOV-based protections, the MAD-based protection, and

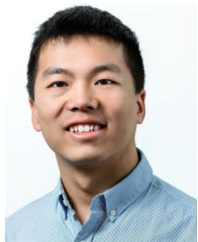
commercial solutions as proposed in [8], [27]. The presented results confirm the proposed protection algorithm's superiority in selectivity and sensitivity.

This work can be extended in four directions. 1) program the proposed protection algorithm in the hardware Field Programmable Gate Array (FPGAs) unit to ensure its experimental verification; 2) carry out the hardware-in-the-loop (HIL) testing of the programmed FPGAs (protective relays) in a cyber-physical real-time digital simulator (RTDS); 3) establish the communications between the relays and other components and formulate the threshold values adaptive to all possible fault conditions and system oscillations, e.g., DCCB reclosing and switching between different MMC control scenarios; 4) find the optimal sampling frequency and threshold value settings to continue improving the sensitivity and selectivity performance by investigating the TW reflection and refraction process.

REFERENCES

- [1] S. S. Mirhosseini, S. Jamali, and M. Popov, "Non-unit protection method for long transmission lines in MTDC grids," *IET Gener., Transmiss. Distrib.*, vol. 15, no. 11, pp. 1674–1687, 2021.
- [2] S. Gao, Q. Liu, and G. Song, "Current differential protection principle of HVDC transmission system," *IET Gener., Transmiss. Distrib.*, vol. 11, no. 5, pp. 1286–1292, 2017.
- [3] T. G. Bolandi, H. Seyedi, S. M. Hashemi, and P. S. Nezhad, "Impedance-differential protection: A new approach to transmission-line pilot protection," *IEEE Trans. Power Del.*, vol. 30, no. 6, pp. 2510–2518, Dec. 2015.
- [4] L. Chen et al., "Similarity comparison based high-speed pilot protection for transmission line," *IEEE Trans. Power Del.*, vol. 33, no. 2, pp. 938–948, Apr. 2018.
- [5] J. Sneath and A. D. Rajapakse, "Fault detection and interruption in an earthed HVDC grid using ROCOV and hybrid DC breakers," *IEEE Trans. Power Del.*, vol. 31, no. 3, pp. 973–981, Jun. 2016.
- [6] J. Liu, N. Tai, and C. Fan, "Transient-voltage-based protection scheme for DC line faults in the multiterminal VSC-HVDC system," *IEEE Trans. Power Del.*, vol. 32, no. 3, pp. 1483–1494, Jun. 2016.
- [7] W. Leterme, J. Beerten, and D. Van Hertem, "Nonunit protection of HVDC grids with inductive DC cable termination," *IEEE Trans. Power Del.*, vol. 31, no. 2, pp. 820–828, Apr. 2016.
- [8] C. Zhang, J. Huang, G. Song, and X. Dong, "Non-unit ultra-high-speed line protection for multi-terminal hybrid LCC/MMC HVDC system and its application research," *IEEE Trans. Power Del.*, vol. 36, no. 5, pp. 2825–2838, Oct. 2021.
- [9] R. Li, L. Xu, and L. Yao, "DC fault detection and location in meshed multiterminal HVDC systems based on DC reactor voltage change rate," *IEEE Trans. Power Del.*, vol. 32, no. 3, pp. 1516–1526, Jun. 2017.
- [10] C. Li, A. M. Gole, and C. Zhao, "A fast DC fault detection method using DC reactor voltages in HVDC grids," *IEEE Trans. Power Del.*, vol. 33, no. 5, pp. 2254–2264, Oct. 2018.
- [11] W. Xiang, S. Yang, G. P. Adam, H. Zhang, W. Zuo, and J. Wen, "DC fault protection algorithms of MMC-HVDC grids: Fault analysis, methodologies, experimental validations, and future trends," *IEEE Trans. Power Electron.*, vol. 36, no. 10, pp. 11245–11264, Oct. 2021.
- [12] S. Yang, W. Xiang, R. Li, X. Lu, W. Zuo, and J. Wen, "An improved DC fault protection algorithm for MMC HVDC grids based on modal-domain analysis," *IEEE Trans. Emerg. Sel. Topics Power Electron.*, vol. 8, no. 4, pp. 4086–4099, Dec. 2020.
- [13] K. Satpathi, Y. M. Yeap, A. Ukil, and N. Gedddada, "Short-time Fourier transform based transient analysis of VSC interfaced point-to-point DC system," *IEEE Trans. Ind. Electron.*, vol. 65, no. 5, pp. 4080–4091, May 2018.
- [14] Z. Zheng, T. Tai, J. S. Thorp, and Y. Yang, "A transient harmonic current protection scheme for HVDC transmission line," *IEEE Trans. Power Del.*, vol. 27, no. 4, pp. 2278–2285, Oct. 2012.
- [15] D. Li, A. Ukil, K. Satpathi, and Y. M. Yeap, "Improved S transform-based fault detection method in voltage source converter interfaced DC system," *IEEE Trans. Ind. Electron.*, vol. 68, no. 6, pp. 5024–5035, Jun. 2021.

- [16] V. A. Lacerda, R. M. Monaro, D. Campos-Gaona, D. V. Coury, and O. Anaya-Lara, "Distance protection algorithm for multiterminal HVDC systems using the Hilbert–Huang transform," *IET Gener., Transmiss. Distrib.*, vol. 14, no. 15, pp. 3022–3032, 2020.
- [17] D. Wang and M. Hou, "Travelling wave fault location algorithm for LCC-MMC-MTDC hybrid transmission system based on Hilbert-Huang transform," *Int. J. Elect. Power Energy Syst.*, vol. 121, 2020, Art. no. 106125.
- [18] O. M. K. K. Nanayakkara, A. D. Rajapakse, and R. Wachal, "Traveling-wave-based line fault location in star-connected multiterminal HVDC systems," *IEEE Trans. Power Del.*, vol. 27, no. 4, pp. 2286–2294, Oct. 2012.
- [19] S. Zhang, G. Zou, C. Wang, J. Li, and B. Xu, "A non-unit boundary protection of DC line for MMC-MTDC grids," *Int. J. Elect. Power Energy Syst.*, vol. 116, 2020, Art. no. 105538.
- [20] B. Li et al., "An improved transient traveling-wave based direction criterion for multi-terminal HVDC grid," *IEEE Trans. Power Del.*, vol. 35, no. 5, pp. 2517–2529, Oct. 2020.
- [21] W. Xiang, S. Yang, L. Xu, J. Zhang, W. Lin, and J. Wen, "A transient voltage-based DC fault line protection scheme for MMC-based DC grid embedding DC breakers," *IEEE Trans. Power Del.*, vol. 34, no. 1, pp. 334–345, Feb. 2019.
- [22] S. Liu et al., "Modeling, experimental validation, and application of VARC HVDC circuit breakers," *IEEE Trans. Power Del.*, vol. 35, no. 3, pp. 1515–1526, Jun. 2020.
- [23] C. Zhang, G. Song, A. S. Meliopoulos, and X. Dong, "Setting-less nonunit protection method for DC line faults in VSC-MTDC systems," *IEEE Trans. Ind. Electron.*, vol. 69, no. 1, pp. 495–505, Jan. 2022.
- [24] S. Yang, W. Xiang, and J. Wen, "An improved DC fault protection scheme independent of boundary components for MMC based HVDC grids," *IEEE Trans. Power Del.*, vol. 36, no. 4, pp. 2520–2531, Aug. 2021.
- [25] C. Zhang, G. Song, T. Wang, L. Wu, and L. Yang, "Non-unit traveling wave protection of HVDC grids using Levenberg–Marquart optimal approximation," *IEEE Trans. Power Del.*, vol. 35, no. 5, pp. 2260–2271, Oct. 2020.
- [26] A. Megahed, A. Moussa, and A. Bayoumy, "Usage of wavelet transform in the protection of series-compensated transmission lines," *IEEE Trans. Power Del.*, vol. 21, no. 3, pp. 1213–1221, Jul. 2006.
- [27] C. Zhang, G. Song, T. Wang, and X. Dong, "An improved non-unit traveling wave protection method with adaptive threshold value and its application in HVDC grids," *IEEE Trans. Power Del.*, vol. 35, no. 4, pp. 1800–1811, Aug. 2020.
- [28] L. Liu, Z. Liu, M. Popov, P. Palensky, and M. A. M. van der Meijden, "A fast protection of multi-terminal HVDC system based on transient signal detection," *IEEE Trans. Power Del.*, vol. 36, no. 1, pp. 43–51, Feb. 2021.



advanced MMC control, and power system interoperability.

Le Liu (Student Member, IEEE) was born in Weinan, China, in 1996. He received the bachelor's degree from the Xi'an University of Technology, Xi'an, China, in 2017, and the M.Sc. degree from the School of Electrical Engineering, Xi'an Jiaotong University, Xi'an, China, and Politecnico di Milano, Milan, Italy, in 2020. He is currently working toward the Ph.D. degree with the Intelligent Electrical Power Grid Group, Delft University of Technology, Delft, The Netherlands. His main research interests include protection and fault location for MTDC power systems,



Belgium. Since January 2020, she has been a tenured Assistant Professor with TU Delft, Faculty of Electrical Engineering, Mathematics and Computer Science in the group Intelligent Electrical Power Grids.

Aleksandra Lekić (Senior Member, IEEE) received the B.Sc, M.Sc, and Ph.D. degrees in electrical engineering from the School of Electrical Engineering, University of Belgrade, Belgrade, Serbia, in 2012, 2013, and 2017, respectively. Between 2012 and 2018, she was a Teaching Assistant with the School of Electrical Engineering, University of Belgrade, and an Assistant Professor from 2018 to 2019. In 2019, she was a Postdoctoral Researcher with the Department of Electrical Engineering, KU Leuven, Leuven, Belgium, and Institute EnergyVille, Genk,



future power systems, and wide-area monitoring and protection. He is a Member of Cigre and actively participated in WG C4.502 and WG A2/C4.39. In 2010, he received the prestigious Dutch Hidde Nijland Prize for extraordinary research achievements. He was the recipient of the IEEE PES Prize Paper Award and IEEE Switchgear Committee Award in 2011 and an Associate Editor for Elsevier's *International Journal of Electrical Power and Energy Systems*. In 2017, together with the Dutch utilities TenneT, Alliander, and Stedin he founded the Dutch Power System Protection Centre to promote research and education in power system protection.

Marjan Popov (Fellow, IEEE) received the Ph.D. degree in electrical power engineering from the Delft University of Technology, Delft, The Netherlands, in 2002. He is a Professor of power system protection with the Delft University of Technology. He is also a Chevening Alumnus and in 1997, he was an Academic Visitor with the University of Liverpool, Liverpool, U.K., working in the Arc Research Group on modeling SF6 circuit breakers. His main research interests include future power systems, large-scale power system transients, intelligent protection for